Materials & Design 245 (2024) 113301

Contents lists available at ScienceDirect

Materials & Design

journal homepage: www.elsevier.com/locate/matdes

Demonstration and benchmarking of a novel powder sheet additive manufacturing approach with austenitic steel

Wenyou Zhang [a,*], Silvia Marola [b], Seán McConnell [c], Zhe Cai [d], JanMell Dugenio [a], Ming Li [e], William M. Abbott [a], Asli Coban [f], Arnoldas Sasnauskas [a], Shuo Yin [a], Ramesh Padamati Babu [f], Wajira Mirihanage [d], Riccardo Casati [c], Rocco Lupoi [a,*]

[a] Trinity College Dublin, The University of Dublin, Department of Mechanical, Manufacturing & Biomedical Engineering, Dublin, Ireland
[b] Politecnico di Milano, Department of Mechanical Engineering, Via la G. La Masa 1, 20156 Milano, Italy
[c] 3CPT, Dublin, Ireland
[d] Department of Materials, The University of Manchester, Manchester M13 9PL, UK
[e] School of Mechanics, Civil Engineering and Architecture, Northwestern Polytechnical University, Xi'an 710072, PR China
[f] Trinity College Dublin, The University of Dublin, School of Chemistry, CRANN & AMBER, Dublin, Ireland

ARTICLE INFO

Keywords:
Powder sheet
Tensile performances
Microstructure
Heat treatment
Laser beam powder bed fusion

ABSTRACT

A novel approach of Metal Additive Manufacturing using Powder Sheet (MAPS) is developed and demonstrated. A flexible metal particle-polymeric binder composite sheet is employed as innovative feedstock in this new method and this approach offers enhanced health and safety. MAPS successfully printed dense samples (99.99%). The chemical composition of the printed alloy resulted enriched in carbon compared to the feedstock powder due to the C pick-up during MAPS, leading to distinct microstructures and enhanced mechanical properties compared to those of laser beam powder bed fusion (PBF-LB/M) benchmark samples. In particular, the microstructural examinations of the MAPS samples show a coarser carbide network stable even after thermal treatment at high temperatures, while the tensile tests revealed that MAPS samples have a higher mechanical strength than the PBF-LB/M counterparts but possess lower ductility. The modification in the chemical composition indicates a strong potential for in-process alloying through MAPS. The demonstrated MAPS approach offers a novel avenue for manufacturing functional metal components with bespoke compositions and resulting properties.

1. Introduction

Additive manufacturing (AM) is a rapidly developing manufacturing method that offers its main advantages in fabricating complex geometries and personalizing designed structures in one step [1–3]. Powder bed fusion (PBF-LB/M) is one of the dominant metal AM methods [4–7]. In metal PBF-LB/M, the particles are sequentially melted by a finely focused energy beam to form a predesigned geometry in a spot-by-spot manner and the 3D structures are built up by adding successive layers of material [8,9]. However, the usage of loose powder feedstock in metal PBF-LB/M has several drawbacks, such as it can potentially cause health risks for the AM machine operators and it is impractical to switch materials and labour intensive to clean the printing chamber after the printing process is complete, which are limiting the wider uptake of PBF-LB/M in industrial environments. To solve these issues, Bodner et al. developed a novel liquid-dispersed metal PBF-LB/M method, wherein a metal suspension (i.e. metal particle-binder) is spread by a re-coater [10]. Despite this advancement, it is challenging to recycle different metallic materials after the printing of components is complete. Therefore, novel AM methods are needed to enhance the safety of feedstock and prevent cross-contamination of the used materials.

Some of the authors have recently designed and developed a novel technical approach for Metal Additive Manufacturing using Powder Sheet (MAPS) that uses powder sheet (i.e. metal particle-polymer composite) as the feedstock [11–14]. In contrast to the conventional PBF-LB/M manufacturing process that employs loose powder as feedstock, MAPS employs a flexible powder sheet as raw material (Fig. 1). Within the powder sheet, a polymeric binder tightly connects the metal particles to avoid the risks associated with using loose powders. The steps involved in the MAPS process are as follows: 1) after an energy beam is activated,

* Corresponding authors at: Trinity College Dublin, The University of Dublin, Department of Mechanical, Manufacturing & Biomedical Engineering, Dublin, Ireland (W. Zhang).
E-mail addresses: zhangw7@tcd.ie (W. Zhang), lupoir@tcd.ie (R. Lupoi).

https://doi.org/10.1016/j.matdes.2024.113301
Received 9 June 2024; Received in revised form 19 July 2024; Accepted 5 September 2024
Available online 7 September 2024

the polymeric binder is vaporized and the metal particles are melted simultaneously; 2) after finishing the fabrication of the pre-designed geometry in a specific layer, the laser beam is switched off and the base plate is moved down by a distance that equals to thickness of solidified material; 3) a fresh area of powder sheet is moved to cover the building platform. The 3D structures are printed by repeating the above processes in a layer-by-layer manner.

The advantages of MAPS over PBF-LB/M include [11]: 1) a significant improvement in the safety of feedstock storage and delivery, due to the usage of powder sheet type of feedstock, instead of the hazardous loose powder used in PBF-LB/M; 2) prevention of cross-contamination of materials in multi-material and functional gradient materials printing, due to the easy change of each feedstock on the input rollers for recycling of unused powder sheets; 3) an improved manufacturing efficiency in printing large-scale metal components, due to the possibility to increase the layer thickness of solidified material by using thicker powder sheet, which can be rapidly changed in minutes; 4) reduced feedstock usage, due to no feedstock surrounding the components to be built is needed; 5) an improved freedom to control the feedstock, allowing for capabilities such as printing in an inclined direction that is similar with the directed energy deposition process, due to that the metal particles are held together by the polymeric binder; 6) low requirement on morphology/flowability of metal powder used for the fabrication of powder sheet [15].

Microstructure plays a crucial role in influencing the mechanical properties of additively manufactured samples [16–18], which have been widely explored [19–21]. In PBF-LB/M printed 304L stainless steel (SS304), fine cellular substructures are typically observed. This microstructure is obtained through the rapid solidification that is involved in the process [22,23]. The results from Zhai et al. indicate that the ultimate tensile stress (UTS) and yield strength of PBF-LB/M as-built SS304 are 706.7 MPa and 454.7 MPa, respectively [24]. The corresponding EBSD mapping results show that the average grain size of PBF-LB/M printed SS304 is 4.9 μm. To relieve the residual stresses arising within the as-built, post-build processing, such as heat treatment (HT), can be operated after the printing of components is complete. Zhang et al. investigated the effect of HT on the microstructural and mechanical characterizations of PBF-LB/M manufactured SS304 [25]. The results showed that the cellular substructures disappeared after a solution annealing at 1050 °C for 2 h, leading to an increase in tensile elongation. As it is a newly proposed method, there has been no knowledge of the microstructures and mechanical performance of MAPS printed samples yet. For the further development of MAPS, it is critical to fundamentally understand the relationship between microstructure and mechanical property arising in this novel manufacturing method.

This study presents the demonstration and analysis of the mechanical performances and underpinning metallurgical aspects of MAPS printed steel. Austenitic steel is utilized as a demonstrating material to investigate the effect of MAPS on a conventional steel grade and to assess the MAPS potential for structural applications across wider industrial requirements. The properties such as density, microstructure, and microhardness of MAPS printed austenitic steel samples are compared to those of the same material printed by PBF-LB/M. The mechanical properties of as-built and heat treated austenitic steel manufactured by MAPS are evaluated for the first time through this contribution and the potential of this novel approach is outlined. The results of this study will facilitate analyses of the applicability of the MAPS process for other metallic and other materials such as ceramics.

2. Method and materials

2.1. MAPS using powder sheet feedstock

To manufacture austenitic steel samples using the MAPS method (Fig. 1), the powder sheet (Fig. 2) was firstly prepared using a “solvent casting method” [11,12,15]. Briefly, a pre-mixed solution was prepared by dissolving PCL $(C_6H_{10}O_2)_n$ pellets in chloroform, followed by mixing with metal particles to form a metal-polymer–solvent dispersion. The dispersion was poured on a flattened casting surface that was moving constantly, on which a 90° bevelled razor blade was incorporated [11]. The setting thickness of the powder sheet is controlled by adjusting the distance between the bottom surface of the razor blade and the top surface of the dispersion. The solvent is evaporated with time, and the metal particle-polymer solidifies to be a film, which is referred to as a powder sheet. Details of the preparation of the powder sheet can be found in the authors’ previous studies [11–13]. The particle size of austenitic steel powder (Carpenter Additive) ranges from 15 to 45 μm. Table 1 shows the chemical composition of austenitic steel powder.

The morphology of the austenitic steel powder sheet is shown in Fig. 2a-b. The PCL binder packs the metal particles tightly so that there is no chance that the powders will get loose at room temperature. The thickness of the austenitic steel powder sheet was measured as 117 ± 5 μm, using a Laserliner machine (CoatingTest-Master, Mitutoyo), which can be adjusted by controlling either the distance between the razor blade and the casting surface or the ratio of metal powder to PCL binder. Thermogravimetric analysis (TGA, Pyris 1 TGA, Perkin Elmer) was performed under a nitrogen environment, heating the samples from 30 to 800 °C at a rate of 10 °C/min [11]. The decomposition behaviour of the austenitic steel powder sheet reveals that the decomposition of PCL is complete after 360 °C, with the weight percentage of austenitic steel remaining constant at 95.72 % from this temperature onward (Fig. 2c). The volume percentage of metal material in the powder sheet is 75.36 %, calculated by mass and density of metal and PCL polymeric binder.

The MAPS process is performed using the Realizer SLM50 system

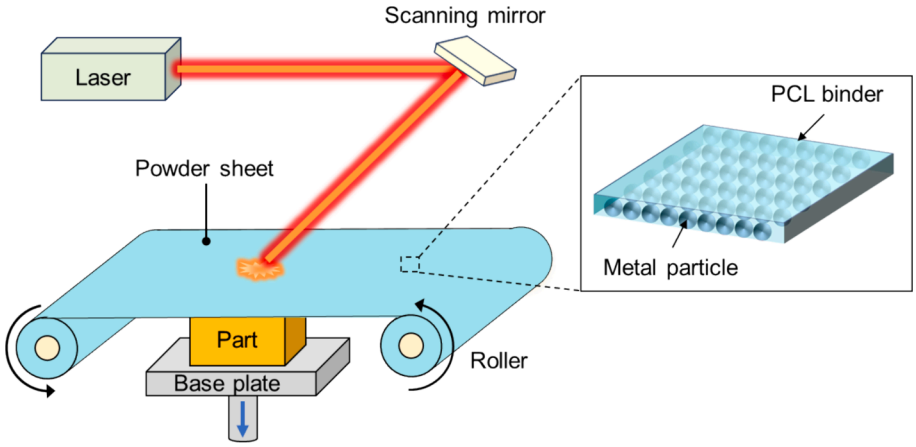

Fig. 1. Schematic illustration of MAPS using powder sheet as feedstock.

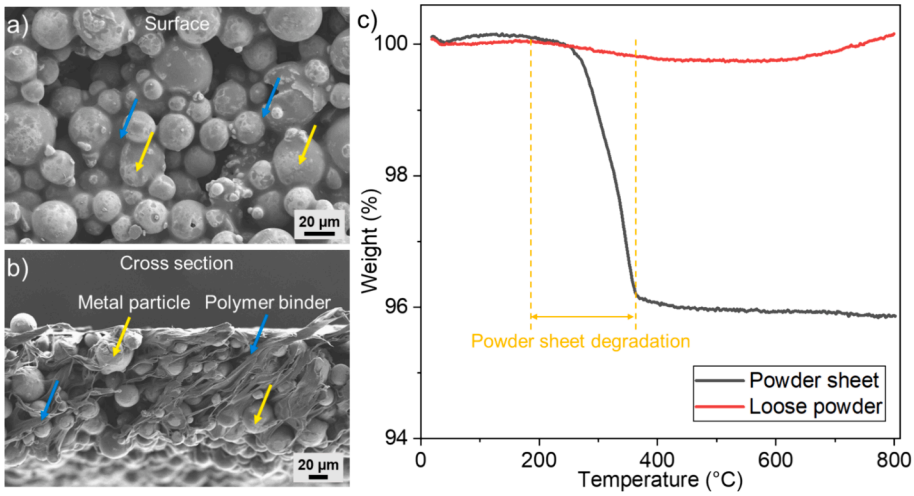

Fig. 2. Characterisations of austenitic steel powder sheet feedstocks: SEM image of the morphology of the powder surface a) and cross-section b) of austenitic steel powder sheet and c) thermogravimetric analysis and a comparison of austenitic steel loose powder and austenitic steel powder sheet.

Table 1
Chemical compositions of austenitic steel loose powder (wt.%).

Si	Cr	Ni	Mn	C	O	S	P	Fe
0.45	19.41	9.78	1.12	0.018	0.037	0.004	0.01	Bal.

(ReaLizer GmbH, Borchen, Germany) after removing the re-coater. A continuous-wave (CW) fibre laser with a 1064 nm wavelength and a Gaussian beam profile is installed in the printing system. For printing of the first layer, the powder sheet material was placed to be directly in contact with the austenitic steel base plate. The laser beam scanned the predefined 50 × 6 mm^2 area. After scanning the first layer, the base plate was lowered by a specific distance of 20 μm, derived from the total deposition height and the number of layers. The average layer thickness is smaller than the thickness of the powder sheet or the metal particle size due to material shrinkage during the melting-solidification processes of metal AM [26]. This distance represents the average layer thickness of solidified material per layer, which correlates with the thickness of the powder sheet. To reposition the powder sheet to be scanned, the purge of the inert gas was paused, allowing for manual adjustment for the powder sheet by operating through the glove box. Then, the printing chamber was pumped again. The printing of the new layer took place after the oxygen level was lower than 0.24 %. The 1.5 mm thick austenitic steel samples were printed by repeating the above processes. Using the specifically designed MAPS system (Fig. 1), which is under development, it will be possible to automatically change the position of the powder sheet feedstock in a few seconds.

To examine the microstructural and mechanical property of MAPS printed components, three 50 × 6 × 1.5 mm^3 samples were printed on an austenitic steel base plate. Considering that the MAPS system is still in a prototype version and the dimensions of the printable samples are limited, to keep consistency between MAPS and PBF-LB/M, 37.5 mm long non-standard tensile samples were designed and printed (Fig. 3).

2.2. PBF-LB/M using loose powder feedstock for benchmark

For the sake of comparison with MAPS, three 50 × 6 × 1.5 mm^3 samples were PBF-LB/M printed as benchmarks. To prevent oxidation, the PBF-LB/M printing was conducted in an argon environment with a consistent inert gas flow rate of 65 L/min. The printing job was performed with an oxygen level in the printing chamber below 0.24 %. A fixed set of process parameters was utilized and reported in Table 2, which has been optimised based on the authors' previous studies [11,12]. Both the MAPS and PBF-LB/M manufactured austenitic steel samples were cut from the base plate by a wire electrical discharge machine (Excetek V440G EDM). HT was performed on both MAPS and PBF-LB/M printed samples at 1040 °C for 2 h, followed by cooling in a vacuum furnace. Subsequently, the as-built and heat-treated samples were EDM machined in the form of dog bone specimens (Fig. 3b) for tensile tests.

2.3. Material analysis and testing

To quantitatively measure the density of MAPS and PBF-LB/M manufactured samples, a representative 5 × 5 × 1 mm^3 specimen was analysed using μ-CT (XT H 225 X-ray System, Nikon Metrology, Hertfordshire, UK) at a resolution of 4.90 μm. The density of samples was also measured using Archimedes' method, according to ASTM B962-17 [27]. The amount of C, O, and N was determined by the LECO elemental

Table 2
Process parameters applied for printing austenitic steel samples for MAPS and PBF-LB/M.

Laser power (W)	Scanning speed (mm/s)	Hatch spacing (μm)	Average layer thickness (μm)
100	200	100	20

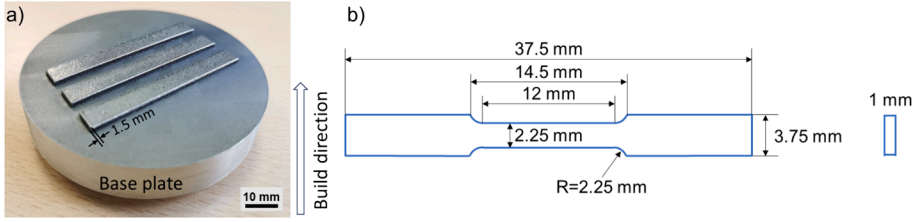

Fig. 3. A) austenitic steel samples printed by maps and b) illustration of the dimension of the samples used for the tensile tests.

analyser (C: C/S 744 model and N, O: ONH 836 model). Thermodynamic calculations were conducted using Thermo-Calc software (Version 2023.1.108587–453 coupled with the TCFE12: Steels/Fe-Alloys v.12.0 database). The microhardness of the austenitic steel samples is measured with $HV_{0.5}$ by keeping a distance of 200 μm between adjacent measurements.

For scanning electron microscopy (SEM, Zeiss ULTRA plus, ZEISS Microscopy, Oberkochen, Germany), Energy-dispersive X-ray spectroscopy (EDS, Oxford Instruments Ultim Max detector coupled with the Aztec software, Abingdon, UK) and electron backscatter diffraction (EBSD, Symmetry S1, Oxford Instrument, Abingdon, UK), the samples were hot mounted in a conductive resin using Metkon Ecopress 50 (Metkon Instruments Inc. Bursa, Turkey), ground using different grades of abrasive sandpapers, and polished using diamond suspensions of 6 μm, 3 μm, and 1 μm. Finally, to achieve a mirror finish, a 0.25 μm silica suspension was employed. To characterize the microstructure of MAPS and PBF-LB/M manufactured austenitic steel using SEM, the polished samples were further etched. The etch of samples was performed using a 1:1:1 solution of distilled water: HNO_3: HCl for 6 s. To check the phases present in MAPS and PBF-LB/M printed austenitic steel, X-ray diffraction (XRD) was performed, with loose powder data as a control. The Rigaku SmartLab SE multipurpose XRD (Rigaku, Tokyo, Japan) is equipped with a Cu radiation source. The measurements were performed in a 2θ range from 20° to 100° at a scanning rate of 1.5°/min and a step size of 0.02° in a Bragg-Brentano geometry.

To investigate the grain size and orientation of MAPS printed as-built and heat treated samples with PBF-LB/M as a benchmark, the Tescan LC electron microscope, equipped with an EBSD detector from Oxford Instruments, was utilized. Characterization covered a defined area of 400 μm by 400 μm, with operational parameters set at an accelerating voltage of 20 kV, a beam current of 28nA, and a scanning step size of 1 μm. Using AZtecCrystal software from Oxford Instruments, the raw EBSD data were analysed for the derivation of the Inverse Pole Figure (IPF), a comparative assessment of grain size distribution, and the texture pole figure. The EBSD analysis was performed along the XY direction, and the reference direction of IPF maps was aligned with the building direction.

Four different sets of samples, including MAPS as-built, PBF-LB/M as-built, MAPS HT, and PBF-LB/M HT, were tested for tensile property using an INSTRON 8801 machine (Instron®, Norwood, USA) at room temperature. After being tested, SEM was performed on the fracture surfaces to determine the failure mode.

3. Results and discussion

3.1. Density characterization

To assess the capability of MAPS in printing dense samples, the density of printed austenitic steel was experimentally determined. μ-CT scanning reveals a high density of both MAPS (99.99 %) and PBF-LB/M (99.95 %) printed samples (Fig. 4). It is worth noting that the minimum defect size that can be discerned by μ-CT is 4.90 μm. Material density was also determined by Archimedes' method. PBF-LB/M printed austenitic steel shows a slightly higher relative density than the MAPS counterpart (7.89 g/cm^3 vs. 7.80 g/cm^3). The difference can be attributed to slight differences in chemical composition (see next section) or in the density of micro-pores.

3.2. Compositional and microstructural characterizations

Fig. 5 shows microstructures developed in the MAPS as-built, PBF-LB/M as-built, MAPS HT, and PBF-LB/M HT samples. The microstructures observed in MAPS differ significantly from those of the PBF-LB/M printed samples. At a lower magnification, the MAPS samples exhibited a cellular microstructure, with a rare occurrence of the side-branches (Fig. 5a). The PBF-LB/M as-built samples show the characteristic fish-scale microstructure of 3D printed alloys, and the hierarchical cell structures appear with the increment of magnification (Fig. 5b). The cellular substructures are retained for the MAPS HT samples (Fig. 5c). The cellular substructures and boundaries between melt pools disappeared for the PBF-LB/M HT samples (Fig. 5d), as a result of the solubilization of the segregated elements enriching cell boundaries and melt pool interfaces [16,21]. The same phenomenon has been reported in other PBF-LB/M studies [16,25]. However, for the MAPS samples, the cellular substructures are retained after HT (Fig. 5d).

EDS mapping reveals distinct microstructures in the samples printed by MAPS and PBF-LB/M (Fig. 6). Samples printed by MAPS show a marked network segregated around the ferrous cells. The cells are composed mainly of Fe and Ni, while the continuous network is enriched in C, Cr, and Mn. It is believed that the ferrous cells, mainly composed of Fe and Ni, are the first ones to solidify and that during the solidification process C, Cr, and Mn are rejected in the liquid, thus originating the network evidenced in the EDS maps (Fig. 6).

Samples printed by PBF-LB/M, on the other hand, show a finer cellular structure surrounded by a fine network slightly enriched in C. After HT, the elemental distribution characterizing the as-built MAPS samples is retained, whereas in the PBF-LB/M samples, all the elements appear homogeneously distributed in the ferrous matrix.

To explain the differences in microstructural properties between MAPS and PBF-LB/M, the contents of C, N, and O were quantitatively measured in both MAPS and PBF-LB/M printed austenitic steel. As visible from Table 3, the MAPS printed austenitic steel samples exhibit a higher content of C than the PBF-LB/M counterparts. This arises from the incorporation of C in the solidified material through the degradation of PCL based polymeric binder during the MAPS process. The C content in the PBF-LB/M printed austenitic steel samples is consistent with the

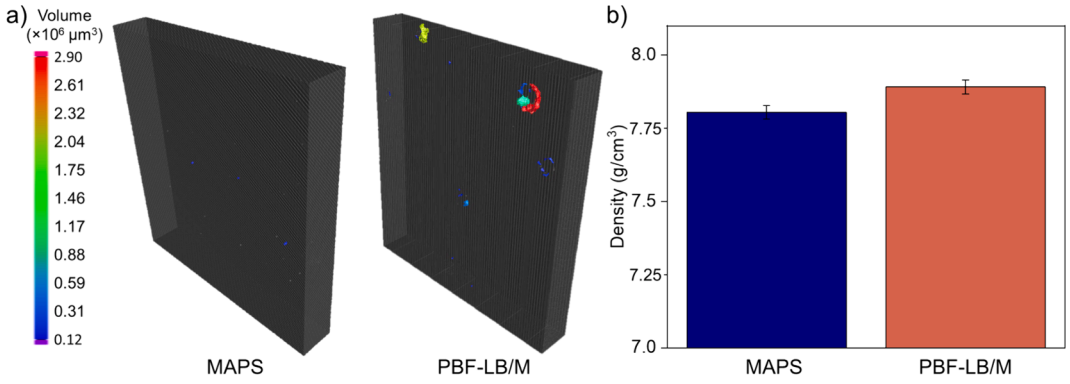

Fig. 4. Density of MAPS and PBF-LB/M printed austenitic steel: a) μ-CT scanning revealing porosity of austenitic steel samples and b) comparison of density measured using Archimede's method.

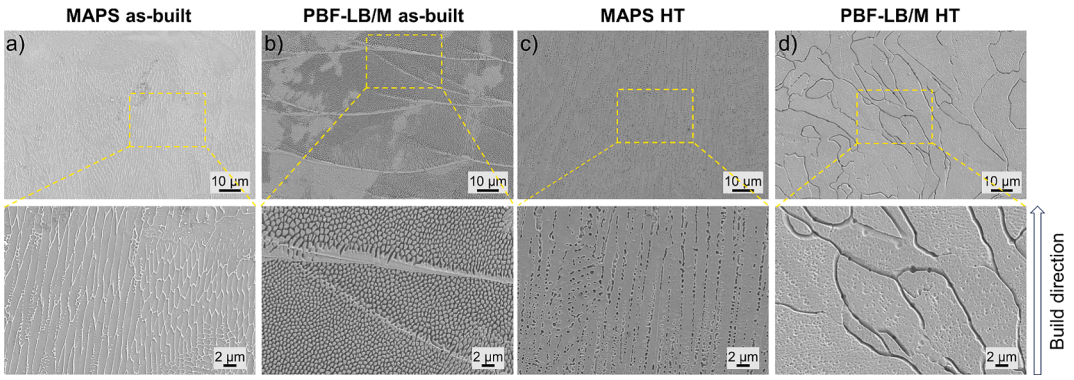

Fig. 5. Comparison of etched microstructure: a) MAPS as-built, b) PBF-LB/M as-built, c) MAPS HT and d) PBF-LB/M HT.

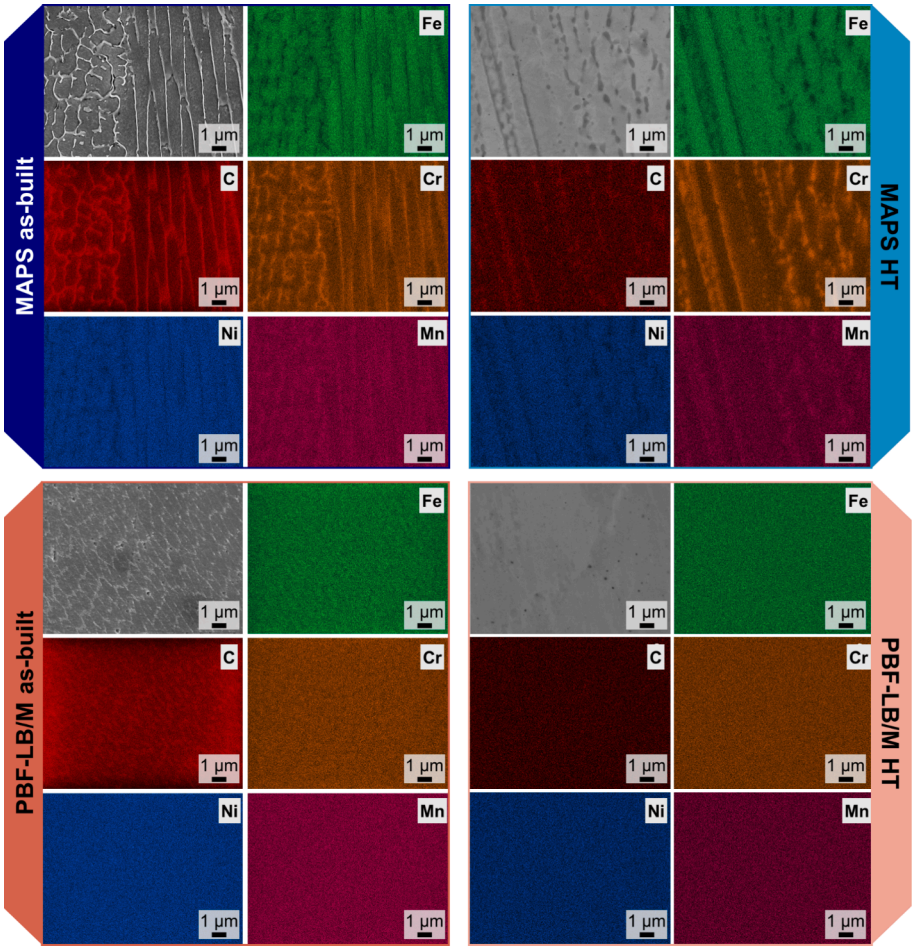

Fig. 6. EDS mapping comparison of the etched microstructure of MAPS and PBF-LB/M printed as-built and HT austenitic steel.

Table 3
Elemental contents in MAPS and PBF-LB/M printed austenitic steel.

	C (wt.%)	N (wt.%)	O (wt.%)
MAPS	1.100	0.058	0.017
PBF-LB/M	0.018	0.063	0.031

composition of the loose powder feedstock (Table 1). Additionally, the O content in both MAPS and PBF-LB/M samples is consistent with the data collected from the loose powder [28]. Due to this change in the chemical composition of the alloy, the MAPS printed material cannot be considered stainless steel of the same grade of PBF-LB/M, so the potential application of this material needs to be completely rethought.

In light of these new results, the Thermo-Calc software was used to predict the phases that form following a non-equilibrium solidification. Scheil-Gulliver hypotheses were assumed for the simulation of the solidification curve. The results (Fig. 7) show that in the alloy processed by MAPS, and so enriched in C content, the first phase to form is the Fe-γ (Fe-FCC) followed by the potential formation of M_7C_3 carbides, while in the sample produced by PBF-LB/M, the only phases that should form are the Fe-α (Fe-BCC) and Fe-γ. These results are in good agreement with the observed micrographs and EDS maps showing segregated C, Cr, and Mn segregated at the cell boundaries of the MAPS sample (Fig. 5 and Fig. 6).

The higher C content, moreover, leads to a significantly higher

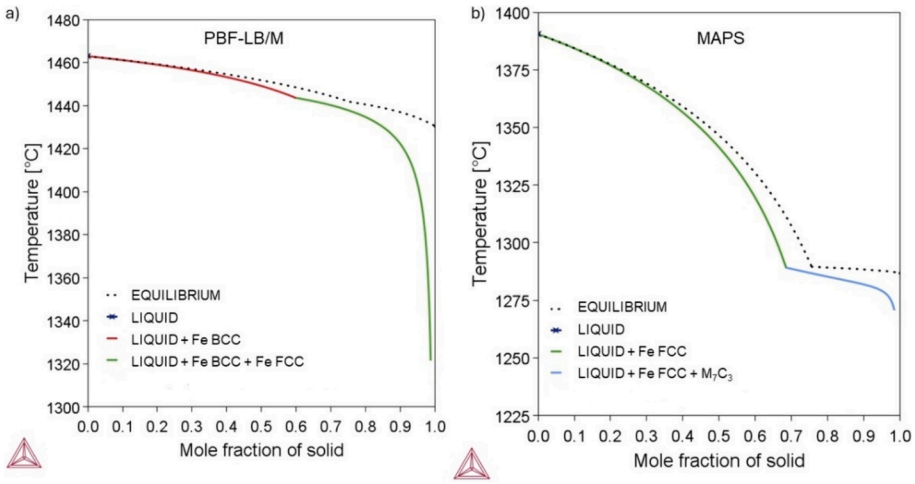

Fig. 7. Equilibrium phase evolution of a) PBF-LB/M and b) MAPS printed samples.

averaged microhardness of the MAPS printed austenitic steel (427 ± 19 $HV_{0.5}$) than PBF-LB/M (231 ± 9 $HV_{0.5}$). The measured microhardness of the PBF-LB/M samples is comparable to the value (233 ± 3 $HV_{0.5}$) reported in other PBF-LB/M study [23]. The higher microhardness and strength can be beneficial for some structural applications or parts subjected to wear. Even though the authors are well aware of the fact that the increase in C leads to different material characteristics, especially in terms of decreased corrosion resistance, in this work, austenitic steel is used as a common steel to demonstrate the feasibility of the process. Thus, corrosion-related properties of the resulting alloy enriched in C are beyond the scope of this work. However, studies regarding effectively reducing the C content in MAPS printed materials are ongoing. It is feasible to fabricate austenitic steel samples with controllable C content (e.g. as low as that of PBF-LB/M) using powder sheet feedstock, and the results will be published as a separate study.

The chemical composition of the representative powder feedstock material corresponds to typical austenitic steel composition of 304L. The XRD pattern of the samples printed by MAPS shows only reflections clearly related to austenite (Fe-γ) with a face-centred cubic (FCC) structure. In contrast, the samples printed by PBF-LB/M show reflections from both FCC austenite and body-centred cubic (BCC) ferrite (Fe-α) (Fig. 8), as expected from the simulation of the solidification under non-equilibrium conditions (Fig. 7). In addition, the peaks related to austenite in the MAPS samples appear to shift towards lower angles, indicating a higher C supersaturation. The absence of the reflection associated with the M_7C_3 carbides in the pattern of the sample printed by MAPS is likely due to the limited volume fraction of such carbides, resulting in unidentifiable diffraction signals with low intensity. Additionally, the reflections of the carbides are expected to appear closer to those of Fe-γ phase reflections and make further difficulty in exact identification.

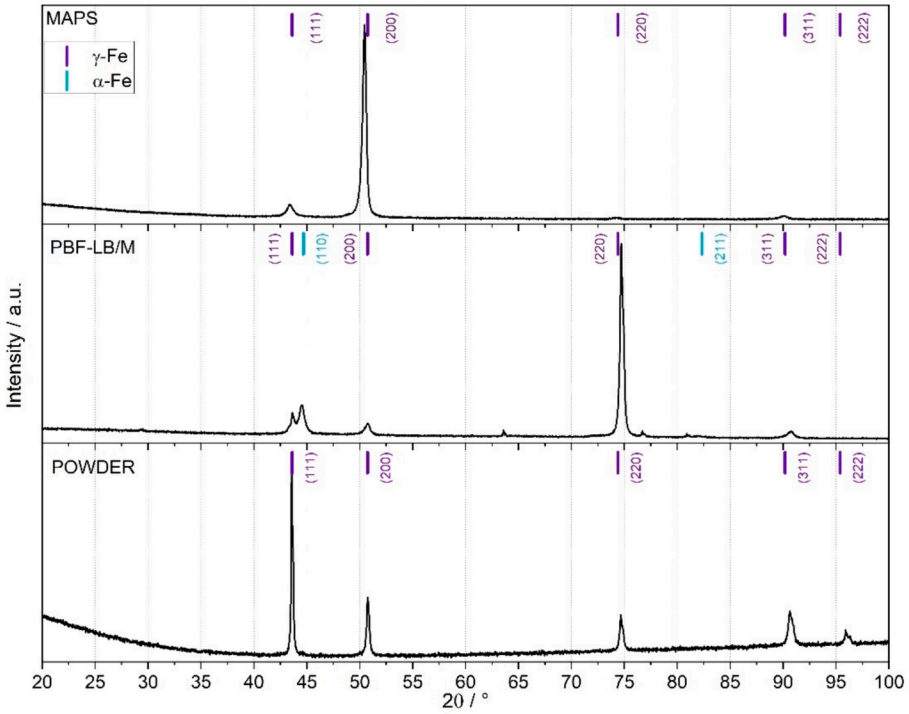

Fig. 8. XRD comparison of austenitic steel loose powder, MAPS and PBF-LB/M printed austenitic steel samples. Not indexed peaks in the pattern related to the PBF-LB/M sample derive from the Al substrate employed during the measurements.

3.3. EBSD analyses

Both as-built and heat treated MAPS specimens show elongated coarse columnar grains oriented along the printing direction (Fig. 9). The average grain sizes for the MAPS as-built and PBF-LB/M samples are 78 ± 4 μm^2 and 48 ± 2 μm^2, respectively. Given that the same process parameters were used to print MAPS and PBF-LB/M samples, the difference in microstructure can be attributed to the presence of the binder, which affects the composition and the solidification of the alloy. A typical zig-zag grain structure was observed in both PBF-LB/M as-built and HT samples. HT at elevated temperatures promotes grain growth, with HT material showing an enlargement by more than 95 % compared to the as-built PBF-LB/M sample. The effect of the polymeric binder on the evolution of the melt pool is visible from the difference in grain size between MAPS and PBF-LB/M, suggesting variations in the thermal gradient experienced during processing. Higher C content in the feedstock material can reduce the Marangoni forces in the melt pool of AM [29–31]. In addition, the evaporation of the polymeric binder may also negatively affect the balance of the driving forces in the overall flow of the melt pool. Thus, the alteration resulting from the inclusion of polymeric binder can influence the evolution of the melt pool and solidification processes, inducing a relatively weaker flow in the melt pools during MAPS compared to PBF-LB/M [29–31].

3.4. Tensile properties

Fig. 10a shows engineering stress–strain curves of MAPS as-built, PBF-LB/M as-built, MAPS HT, and PBF-LB/M HT samples. Significantly higher UTS is obtained for the MAPS as-built samples (1109 ± 57 MPa) than the PBF-LB/M as-built counterparts (622 ± 9 MPa), as shown in Fig. 10b. The tensile curve of PBF-LB/M printed as-built and the UTS values obtained in this study are similar to those reported in other studies [23,24,28]. The slight variation in literature data can be attributed to the different energy density inputs. After HT, the UTS decreases to 988 ± 7 MPa and 597 ± 8 MPa for MAPS and PBF-LB/M, respectively, which is due to microstructure coarsening after HT [32]. The decrease of UTS after HT compared to the as-built counterparts is shown in Fig. 10b.

For both the MAPS and PBF-LB/M printed samples, the yield strength decreased after HT, compared to the as-built counterparts. The as-built austenitic steel printed by MAPS exhibited an over 100 % higher yield strength (922 ± 10 MPa) than that of the PBF-LB/M (425 ± 21 MPa) counterparts, as shown in Fig. 10c. The heat-treated samples printed by MAPS (432 ± 42 MPa) have a similar magnitude of yield strength with that of the as-built PBF-LB/M manufactured counterparts. The yield strength of heat treated austenitic steel printed by PBF-LB/M decreased to 334 ± 25 MPa. The decrease in the yield strength is due to the grain growth and disappearance of the cellular substructures after HT [21,25,33], which allows for greater plasticity by reducing the barriers to dislocation motion. In addition, the recovery and recrystallization lead to a decrease in dislocation density and strain hardening.

The tensile tests revealed a lower ductility of MAPS printed samples than that of the PBF-LB/M. Fig. 10d shows the elongation of MAPS (22 ± 4 %) printed austenitic steel samples is only 38.60 % of the PBF-LB/M (57 ± 6 %) counterpart. After HT, the elongation of MAPS and PBF-LB/M printed samples increased to 38 ± 3 % and 78 ± 5 %, respectively. This increment in the mechanical properties of the MAPS is to be ascribed to the different chemical composition of the alloy due to the incorporation of C deriving from the degradation of the PCL binder. In fact, the continuous carbide network formed around the austenitic cells in the MAPS sample can pin the dislocation movement leading to an increase in YS and UTS and, conversely, to a decrease in elongation and toughness.

To understand the failure mechanism and to further characterize the tensile performances of the samples, the fracture surfaces of all samples are analysed. The fracture surface of the PBF-LB/M printed austenitic steel indicates a ductile fracture progressing through micro-void coalescence. For both the as-builts and heat-treated samples, a considerable reduction in area is observed in the PBF-LB/M samples compared to that

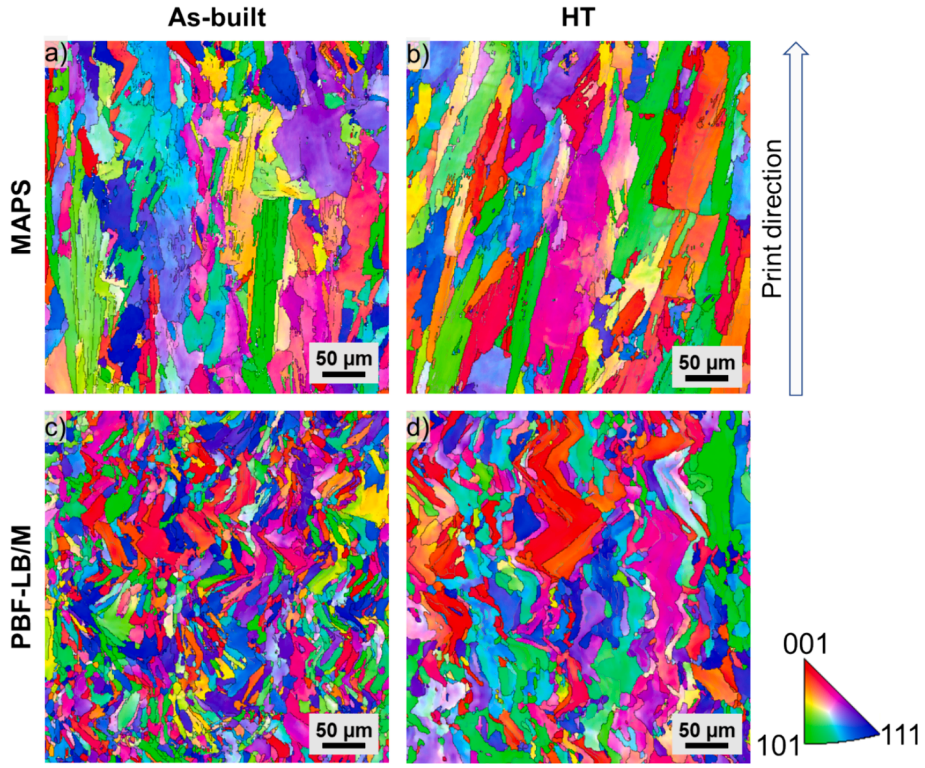

Fig. 9. Inverse pole figure (IPF-Z) mapping of pre-tensile samples printed by MAPS and PBF-LB/M: a) MAPS as-built, b) MAPS HT, c) PBF-LB/M as-built and d) PBF-LB/M HT.

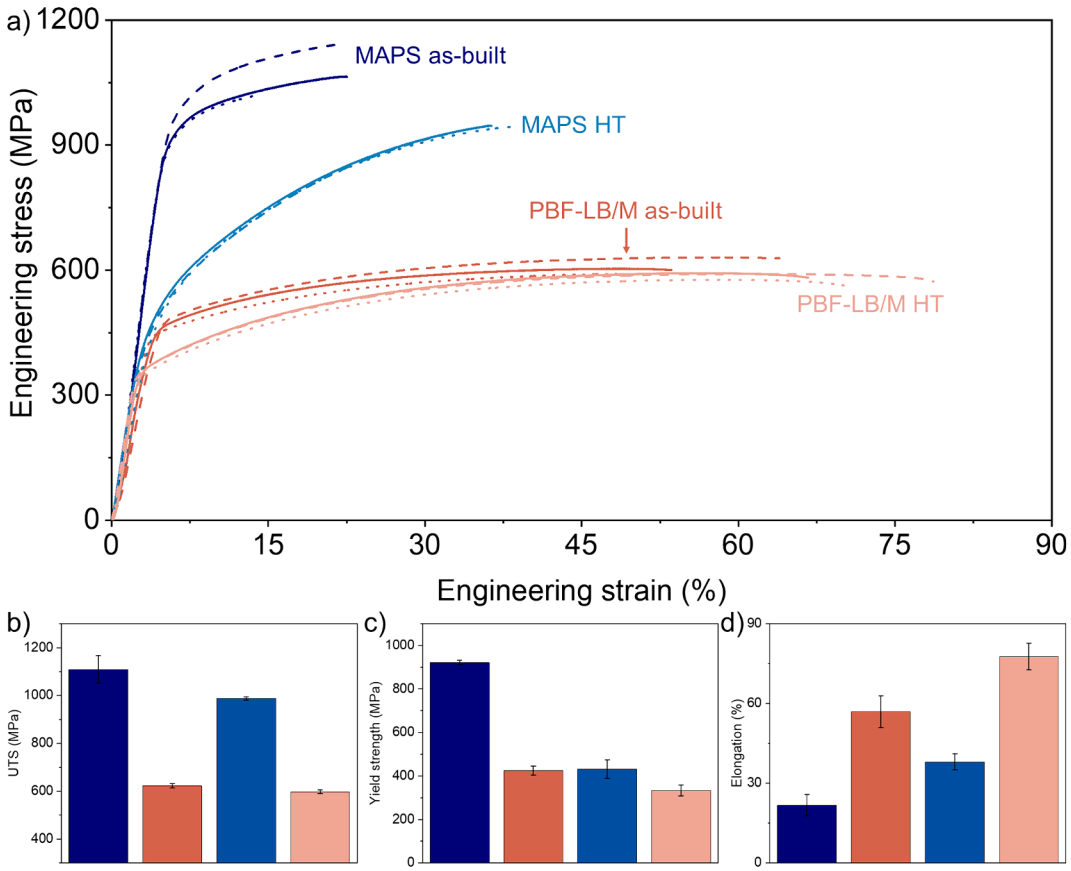

Fig. 10. Tensile test results: a) engineering stress–strain curve, comparisons of b) UTS, c) yield strength and d) elongation of samples printed by MAPS and PBF-LB/M, both as-built and heat treated.

of the MAPS samples, which is a result of necking prior to fracture. Dimples are also observed in the fracture surface of MAPS samples, but they are interspersed with cleavage-type fracture surfaces along the cell boundaries, which is typical of a quasi-cleavage fracture (Fig. 11 a-c). Although there are areas where some dimples or ductile-type features are observed in both samples, the predominance of quasi-cleavage features along with shallow dimples in the MAPS printed samples (Fig. 11 a-c) strongly support that the fracture mode is more brittle in these samples than in the PBF-LB/M counterparts (Fig. 11 d-f). On the fracture surface of the PBF-LB/M samples, dimples are observed together with voids and pores (Fig. 11 d-f). However, the presence of small pores in PBF-LB/M printed samples does not significantly affect the strength or ductility of the samples (Fig. 11). Higher magnification of SEM images in Fig. 11f reveals that the fracture surfaces are predominantly dimples with sizes smaller than 2 μm.

It is interesting to see the fracture surface of heat-treated samples printed by MAPS is flatter and more homogeneous than the PBF-LB/M printed samples. After HT, there are no obvious defects such as pores in either MAPS or PBF-LB/M printed samples (Fig. 11 g-i). In the heat treated PBF-LB/M printed austenitic steel, there are dimples, indicating the occurrence of a ductile fracture. The size of dimples is larger than that of their as-built counterparts.

The different behaviours of the MAPS and PBF-LB/M samples upon thermal treatment are confirmed by simulating the equilibrium phases evolution with temperature using the Thermo-Calc software, as shown in Fig. 12. The results obtained validate that only the FCC austenite is stable in the PBF-LB/M samples (Fig. 12a) at 1040 °C; while at the same temperature, due to the higher C content, in the MAPS samples (Fig. 12b), apart from the austenite stabilization, the presence of stable carbides retained in the matrix is expected.

4. Conclusions

MAPS is a new metal AM approach that utilizes a powder sheet as feedstock that offers enhanced safety and material contamination prevention in comparison to the established PBF-LB/M technique. Process demonstrations of the MAPS printed as-built and heat treated austenitic steel were performed by assessing the mechanical performances of the build samples, considering tensile properties, microstructure, density, microhardness, and were analysed with the benchmark PBF-LB/M results. The key conclusions include:

1) MAPS is experimentally validated as an effective method to manufacture functional metal components using a safer feedstock of powder sheet (i.e. metal particle-polymeric binder composite).
2) MAPS printed samples exhibit near full density (e.g. over 99.99 %). The significantly higher microhardness in MAPS printed austenitic steel samples can be attributed to the significantly higher C content present in the MAPS printed austenitic steel. The increased C content is caused by the decomposition of the PCL binder during MAPS printing. M_7C_3 carbides were formed in the MAPS manufactured sample.
3) Microstructure-property relationship in both MAPS is investigated. Remarkable differences in microstructures are observed between MAPS and PBF-LB/M printed samples. Hierarchical cell structures are visible in PBF-LB/M as-built, whereas the MAPS as-built exhibits elongated columnar substructures.
4) EBSD results revealed that the average grain size of MAPS is 62.89 % higher than that of the PBF-LB/M benchmark in the as-built state. The MAPS printed samples exhibit elongated columnar grains and a broader grain size distribution than PBF-LB/M. This is caused by the

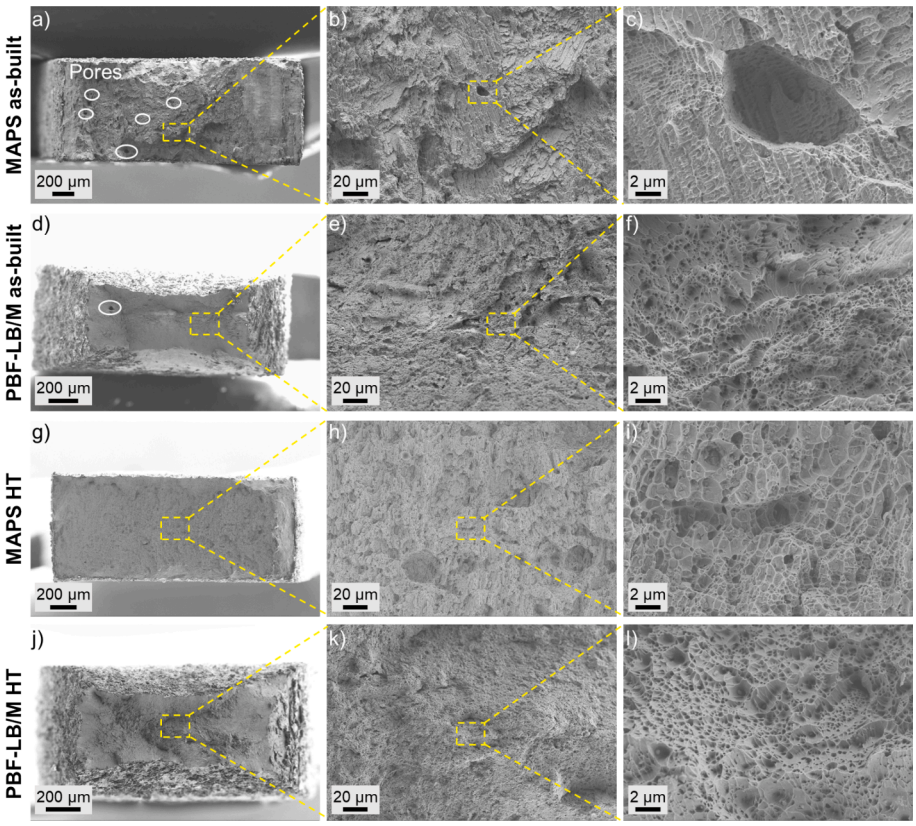

Fig. 11. SEM observation for fracture surface morphology after tensile tests: a)-c) MAPS as-built, d)-f) PBF-LB/M as-built, g)-i) MAPS HT and j)-l) PBF-LB/M HT.

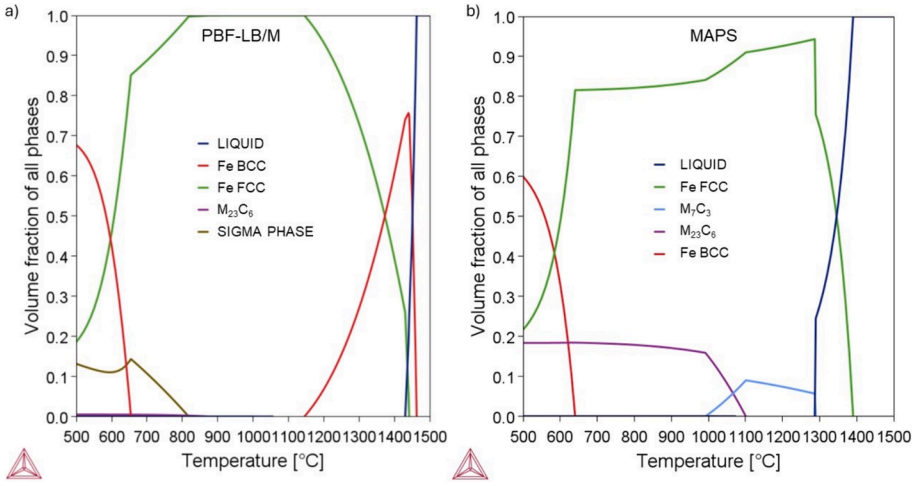

Fig. 12. Equilibrium phase evolution of a) PBF-LB/M and b) MAPS printed samples.

inclusion of polymeric binder resulted in the variation of composition, temperature gradient and solidification rate.

5) The tensile properties of MAPS printed samples are explored for the first time and compared with the benchmark of PBF-LB/M. The UTS of MAPS as-built doubles compared to the PBF-LB/M, but the elongation is only one-third. After HT, the UTS of MAPS samples marginally decreased by 4.02 %. However, the elongation increased by 36.84 %, compared to the as-built samples. This is caused by the change in the chemical composition (mainly C content) in the MAPS printed samples.
6) The demonstrated MAPS approach indicates the capability to modify the chemical composition of functional metal components and provides further insights into the intricate in-process alloying of more advanced materials.

In this study, a higher C content is experimentally detected in the MAPS printed samples, originating from the PCL polymetric binder in the powder sheet feedstock. In future, more advanced material designs with flexible control of the chemical composition can be MAPS manufactured by adjusting the content of the polymeric binder in the powder sheet. HT has been proven to effectively improve the elongation of MAPS manufactured SS304 by 72.73 % compared to the as-built state. Further strategies to mitigate the C content and to enhance the elongation of MAPS printed S304 need to be explored.

CRediT authorship contribution statement

Wenyou Zhang: Writing – review & editing, Writing – original draft, Methodology, Investigation, Conceptualization. **Silvia Marola:** Writing – original draft, Investigation. **Seán McConnell:** Investigation. **Zhe Cai:** Investigation. **JanMell Dugenio:** Investigation. **Ming Li:** Investigation. **William M. Abbott:** Investigation. **Asli Coban:** Investigation. **Arnoldas Sasnauskas:** Investigation. **Shuo Yin:** Writing – review & editing. **Ramesh Padamati Babu:** Writing – review & editing. **Wajira Mirihanage:** Writing – review & editing. **Riccardo Casati:** Writing – review & editing. **Rocco Lupoi:** Writing – review & editing, Resources, Project administration, Conceptualization.

Declaration of competing interest

The authors declare that they have no known competing financial interests or personal relationships that could have appeared to influence the work reported in this paper.

Data availability

Data will be made available on request.

Acknowledgements

The authors grateful acknowledge the funding by PosAddive – Powder Sheet Additive Manufacturing (co-funded by EIT RawMaterials, No. 22021), Enterprise Ireland (CF-2020-1564-A/B), Science Foundation Ireland (18/EPSRC-CDT/3581), Engineering and Physical Sciences Research Council (EP/S023259/1), and MICS (Made in Italy – Circular and Sustainable) Extended Partnership and received funding from Next-GenerationEU (Italian PNRR – M4 C2, Invest 1.3 – D.D. 1551.11-10-2022, PE00000004). The authors also acknowledge the National Heat Treatment Centre Ltd for performing heat treatment. EIT RawMaterials is supported by EIT, a body of the European Union.

References

[1] L. Hirt, A. Reiser, R. Spolenak, T. Zambelli, Additive Manufacturing of Metal Structures at the Micrometer Scale, Adv. Mater. 29 (17) (2017) 1604211.
[2] A.K. Ball, A. Basak, Numerical Investigation of the Thermal Distortion in Multi-Laser Powder Bed Fusion (ML-PBF) Additive Manufacturing of Inconel® 625, Chinese Journal of Mechanical Engineering: Additive Manufacturing Frontiers (2023) 100103.
[3] X. Lu, W. Zhang, M. Chiumenti, M. Cervera, B. Gillham, P. Yu, S. Yin, X. Lin, R. P. Babu, R. Lupoi, Crack-free laser powder bed fusion by substrate design, Addit. Manuf. 59 (2022) 103149.
[4] D. Wu, C. Song, T. Di, F. Niu, G. Ma, Intermetallic regulation mechanism of inconel 718/Ti6Al4V composite by novel follow-up ultrasonic assisted laser additive manufacturing, Compos. B Eng. 235 (2022) 109736.
[5] S. Zhang, L. Wang, X. Lin, H. Yang, W. Huang, The formation and dissolution mechanisms of Laves phase in Inconel 718 fabricated by selective laser melting compared to directed energy deposition and cast, Compos. B Eng. 239 (2022) 109994.
[6] W. Zhang, M. Tong, N.M. Harrison, Resolution, energy and time dependency on layer scaling in finite element modelling of laser beam powder bed fusion additive manufacturing, Addit. Manuf. 28 (2019) 610–620.
[7] Q. Wang, W. Zhang, S. Li, M. Tong, W. Hou, H. Wang, Y. Hao, N.M. Harrison, R. Yang, Material Characterisation and Computational Thermal Modelling of Electron Beam Powder Bed Fusion Additive Manufacturing of Ti2448 Titanium Alloy, Materials 14 (23) (2021) 7359.
[8] W. Zhang, M. Tong, N.M. Harrison, Scanning strategies effect on temperature, residual stress and deformation by multi-laser beam powder bed fusion manufacturing, Addit. Manuf. 36 (2020) 101507.
[9] W. Zhang, D. Guo, L. Wang, C.M. Davies, W. Mirihanage, M. Tong, N.M. Harrison, X-ray diffraction measurements and computational prediction of residual stress mitigation scanning strategies in powder bed fusion additive manufacturing, Addit. Manuf. 61 (2023) 103275.
[10] S.C. Bodner, L.T.G. van de Vorst, J. Zalesak, J. Todt, J.F. Keckes, V. Maier-Kiener, B. Sartory, N. Schell, J.W. Hooijmans, J.J. Saurwalt, J. Keckes, Inconel-steel multilayers by liquid dispersed metal powder bed fusion: Microstructure, residual stress and property gradients, Addit. Manuf. 32 (2020) 101027.
[11] W. Zhang, X. Lu, A. Coban, M. Cervera, M. Chiumenti, A. Sasnauskas, C. Huang, S. Yin, R.P. Babu, R. Lupoi, Powder sheet additive manufacturing of multi-material structures: Experimental and computational characterizations, Compos. B Eng. 272 (2024) 111203.
[12] W. Zhang, A. Sasnauskas, A. Coban, S. Marola, R. Casati, S. Yin, R.P. Babu, R. Lupoi, Powder sheets additive manufacturing: Principles and capabilities for multi-material printing, Additive Manufacturing Letters 8 (2024) 100187.
[13] W. Zhang, D. Pullini, M. Alberghini, A. Bertinetti, A. Tommasi, A. Coban, S. McConnell, H. Naesstroem, R.P. Babu, J. Volpp, R. Lupoi, Material incorporation in powder sheet additive manufacturing toward lightweight designs for future mobility, J. Laser Appl. 36 (2) (2024).
[14] W. Zhang, W.M. Abbott, A. Sasnauskas, A. Coban, B. Gillham, I. Bitharas, S. Lu, J. Quirke, S. Ruan, K. Perkins, K. Synnatschke, M. Moebius, S. Yin, A. Moore, R. P. Babu, R. Lupoi, Development of a novel powder sheets printing process towards the next generation of additive manufacturing: the role of laser defocusing, Virtual and Physical Prototyping 19 (1) (2024) e2361856.
[15] W. Zhang, A. Coban, A. Sasnauskas, Z. Cai, B. Gillham, W. Mirihanage, S. Yin, R. P. Babu, R. Lupoi, A novel powder sheet laser additive manufacturing method using irregular morphology feedstock, CIRP J. Manuf. Sci. Technol. 52 (2024) 26–35.
[16] T. Ronneberg, C.M. Davies, P.A. Hooper, Revealing relationships between porosity, microstructure and mechanical properties of laser powder bed fusion 316L stainless steel through heat treatment, Mater. Des. 189 (2020) 108481.
[17] D. Wang, Y. Feng, L. Liu, X. Wei, Y. Yang, P. Yuan, Y. Liu, C. Han, Y. Bai, Influence Mechanism of Process Parameters on Relative Density, Microstructure, and Mechanical Properties of Low Sc-Content Al-Mg-Sc-Zr Alloy Fabricated by Selective Laser Melting, Chinese Journal of Mechanical Engineering: Additive Manufacturing Frontiers 1 (4) (2022) 100034.
[18] L. Zhu, Y. Xu, S. Liu, H. Chen, J. Tao, X. Tong, Y. Li, S. Huang, J. Lin, C. Wen, J. Ma, Microstructure, mechanical properties, friction and wear performance, and cytotoxicity of additively manufactured zirconia-toughened alumina for dental applications, Compos. B Eng. 250 (2023) 110459.
[19] Y. Zhang, W. Huang, Comparisons of 304 austenitic stainless steel manufactured by laser metal deposition and selective laser melting, J. Manuf. Process. 57 (2020) 324–333.
[20] N. Jeyaprakash, C.-H. Yang, K.R. Ramkumar, Correlation of Microstructural Evolution with Mechanical and Tribological Behaviour of SS 304 Specimens Developed Through SLM Technique, Met. Mater. Int. 27 (12) (2021) 5179–5190.
[21] M. Laleh, E. Sadeghi, R.I. Revilla, Q. Chao, N. Haghdadi, A.E. Hughes, W. Xu, I. De Graeve, M. Qian, I. Gibson, M.Y. Tan, Heat treatment for metal additive manufacturing, Prog. Mater Sci. 133 (2023) 101051.
[22] H. Zhang, M. Xu, P. Kumar, C. Li, W. Dai, Z. Liu, Z. Li, Y. Zhang, Enhancement of fatigue resistance of additively manufactured 304L SS by unique heterogeneous microstructure, Virtual and Physical Prototyping 16 (2) (2021) 125–145.
[23] M. Ghayoor, K. Lee, Y. He, C.-H. Chang, B.K. Paul, S. Pasebani, Selective laser melting of 304L stainless steel: Role of volumetric energy density on the microstructure, texture and mechanical properties, Addit. Manuf. 32 (2020) 101011.
[24] W. Zhai, W. Zhou, Z. Zhu, S.M.L. Nai, Selective Laser Melting of 304L and 316L Stainless Steels: A Comparative Study of Microstructures and Mechanical Properties, steel research international 93(7) (2022) 2100664.
[25] H. Zhang, C. Li, G. Yao, Y. Shi, Y. Zhang, Effect of annealing treatment on microstructure evolution and deformation behavior of 304 L stainless steel made by laser powder bed fusion, Int. J. Plast 155 (2022) 103335.
[26] S.L. Sing, S. Huang, G.D. Goh, G.L. Goh, C.F. Tey, J.H.K. Tan, W.Y. Yeong, Emerging metallic systems for additive manufacturing: In-situ alloying and multi-metal processing in laser powder bed fusion, Prog. Mater Sci. 119 (2021) 100795.
[27] B. Gillham, A. Yankin, F. McNamara, C. Tomonto, D. Taylor, R. Lupoi, Application of the Theory of Critical Distances to predict the effect of induced and process inherent defects for SLM Ti-6Al-4V in high cycle fatigue, CIRP Ann. 70 (1) (2021) 171–174.
[28] T. Pan, X. Zhang, A. Flood, S. Karnati, W. Li, J. Newkirk, F. Liou, Effect of processing parameters and build orientation on microstructure and performance of AISI stainless steel 304L made with selective laser melting under different strain rates, Mater. Sci. Eng. A 835 (2022) 142686.
[29] L.T. Hoai, J. Lee, Effect of surface adsorption of carbon on the surface tension of liquid Fe–Mn–C alloys, J. Mater. Sci. 47 (24) (2012) 8303–8307.
[30] D. Guo, K. Yan, M.D. Callaghan, D. Daisenberger, M. Chatterton, J. Chen, A. Wisbey, W. Mirihanage, Solidification microstructure and residual stress correlations in direct energy deposited type 316L stainless steel, Mater. Des. 207 (2021) 109782.
[31] L. Aucott, H. Dong, W. Mirihanage, R. Atwood, A. Kidess, S. Gao, S. Wen, J. Marsden, S. Feng, M. Tong, T. Connolley, M. Drakopoulos, C.R. Kleijn, I. M. Richardson, D.J. Browne, R.H. Mathiesen, H.V. Atkinson, Revealing internal flow behaviour in arc welding and additive manufacturing of metals, Nat. Commun. 9 (1) (2018) 5414.
[32] I. Morozova, C. Kehm, A. Obrosov, Y. Yang, K.U.M. Miah, E. Uludintceva, S. Fritzsche, S. Weiß, V. Michailov, On the Heat Treatment of Selective-Laser-Melted 316L, J. Mater. Eng. Perform. 32 (10) (2023) 4295–4305.
[33] H. Lu, J. Pan, Y. Gu, J. Xiao, C. Ma, N. Yu, H. Li, Comparison of melt evolution and flow mechanisms of Inconel 718, Ti6Al4V, 304 stainless steel, and AlSi10Mg manufactured by laser powder bed fusion, structures, and properties after heat treatments, Mater. Sci. Eng. A 865 (2023) 144649.